Du, Luojun; Molas, Maciej R.; Huang, Zhiheng; Zhang, Guangyu; Wang, Feng; Sun, Zhipei

Moiré photonics and optoelectronics

Published in:
Science

DOI:
10.1126/science.adg0014

Published: 31/03/2023

Document Version
Peer-reviewed accepted author manuscript, also known as Final accepted manuscript or Post-print

Moiré photonics and optoelectronics

Luojun Du[1,2,3]*, Maciej R. Molas[4], Zhiheng Huang[2,3], Guangyu Zhang[2,3,5]*, Feng Wang[6], Zhipei Sun[1,7]*

[1]QTF Centre of Excellence, Department of Electronics and Nanoengineering, Aalto University, Tietotie 3, FI-02150, Finland

[2]Beijing National Laboratory for Condensed Matter Physics; Key Laboratory for Nanoscale Physics and Devices, Institute of Physics, Chinese Academy of Sciences, Beijing, 100190, China

[3]School of Physical Sciences, University of Chinese Academy of Sciences, Beijing 100190, China

[4]Institute of Experimental Physics, Faculty of Physics, University of Warsaw, ul. Pasteura 5, 02-093, Warsaw, Poland

[5]Songshan-Lake Materials Laboratory, Dongguan, Guangdong Province 523808, China

[6]Department of Physics, University of California at Berkeley, Berkeley, CA, USA

[7]Institute of Photonics and Photon Technology, Northwest University, Xi'an 710069, China

*Corresponding authors. Email: zhipei.sun@aalto.fi; luojun.du@iphy.ac.cn; gyzhang@iphy.ac.cn

Abstract: Moiré superlattices, the artificial quantum materials, have provided a wide range of possibilities for the exploration of completely new physics and device architectures. In this Review, we focus on the recent progress on emerging moiré photonics and optoelectronics, including but not limited to moiré excitons/trions/polaritons, resonantly hybridized excitons, reconstructed collective excitations, strong mid-/far-infrared photoresponses, terahertz single-photon detection, and symmetry breaking optoelectronics. We also discuss the future opportunities and research directions in this field, such as developing advanced techniques to probe the emergent photonics and optoelectronics in an individual moiré supercell, exploring new ferroelectric/magnetic/multiferroic moiré systems, and utilizing external degrees of freedom to engineer moiré properties for exciting physics and potential technological innovations.

Main Text: Two-dimensional (2D) layered materials have ushered in a new era of fundamental research and technological innovation, due to the electronic/photonic/optoelectronic properties that are unattainable in their bulk counterparts (1-3). Today, over two-thousand atomically thin 2D materials have been uncovered, ranging from wide-bandgap insulators (e.g., *h*-BN), semiconductors (e.g., MoS_2), and polar metals (e.g., Ga) to superconductors (e.g., $NbSe_2$), ferromagnets (e.g., CrI_3), and quantum spin liquids (e.g., $RuCl_3$) (1, 4-7). Remarkably, 2D atomic layers with diverse properties can be stacked together to form van der Waals (vdW) heterostructures without the constraint of lattice matching in conventional heterostructures. This enables opportunities to combine the best characteristics of different ingredients in one ultimate synthetic quantum material, and thus leads to the realization of numerous electronic, photonic, magnetic, and topological functionalities that were previously impossible (1, 2, 8, 9).

Intriguingly, a geometrical moiré superlattice emerges as a result of the interference between the constituent 2D atomic layers with a slight lattice mismatch and/or a small rotational twist (Fig. 1A) (10, 11). This moiré superlattice introduces a new length and energy scale, and provides a platform to engineer the band structures (including both single-particle states and collective excitations, Fig. 1B) and the light-matter interaction for exotic quantum phenomena (12-16). Triggered by the discovery of correlated insulator states and unconventional superconductivity in magic-angle twisted bilayer graphene (TBG) (17, 18), a plethora of exciting electronic, optical, and optoelectronic properties have been discovered in moiré superlattices (Fig. 1C), including moiré excitons (19-22), versatile quantum light sources (23), orbital ferromagnetism (24-26), Wigner crystal states (11, 27, 28), stripe phases (29, 30), topological multiferroic order (31), boson exciton crystals (32), and intelligent infrared sensing (33).

We present an overview of the recent progress on emerging moiré photonics and optoelectronics, such as moiré neutral/charged excitons, resonantly hybridized excitons, moiré polaritons, emergent optical responses of moiré correlated electronic states, reconstructed collective excitations, terahertz single-photon detection, strong mid-/far-infrared photoresponses, symmetry breaking optoelectronics, etc. We also provide an outlook on the major challenges and future opportunities in this field, as well as the implications for potential new technological innovations. With a particular focus on moiré photonics and optoelectronics, our aim is to complement other recent reviews that discuss the fabrication (34), correlated electronic states (10, 13), and excitonic physics (12, 35, 36).

Fabrication and visualization of moiré superlattices

The controlled fabrication and direct visualization of moiré superlattices are essential for unlocking their intriguing electronic/optical properties and future on-demand application development.

Fabrication of moiré superlattices

Top-down methods: One top-down method for preparing high-quality homobilayer moiré superlattices is the 'tear-and-stack' technique (37, 38). This technique is based on the deterministic pick-up and transfer, and consists of selectively picking up a section of a 2D material, and then transferring it onto the remaining section, which has been rotated by a user-designed angle (34, 38). Because the two constituent layers initially have exactly the same crystal orientation, the twist angle can be controlled with a sub-degree resolution. By pre-determining the principal crystallographic directions of 2D materials, moiré heterostructures with controllable twist angles can also be fabricated via the deterministic pick-up and transfer technique (34). Until now, we have at our disposal a wide variety of moiré homo- and heterostructures, such as twisted transition-

metal dichalcogenide (TMDC) homobilayers (39, 40), twisted bilayer CrI_3 (41, 42), $MoSe_2/WSe_2$ (19, 21), and WS_2/WSe_2 (20, 43). It is noteworthy that an automated robotic pick-up and transfer technique has been recently developed, enabling the rapid manufacture of moiré superlattices with deliberate design and angle control (44, 45). We envision that the advanced robotic assembly, through integration with wafer-scale 2D material growth, machine learning and computer-vision algorithms (46, 47), could help realize the full potential of moiré superlattices for novel physics and technological advances in photonics and optoelectronics.

Bottom-up methods: Developing direct growth methods for synthesizing large-scale and uniform moiré superlattices is important for future technological applications. One of the effective bottom-up methods is the vdW epitaxy (48). For example, a vast assortment of moiré superlattices with ultra-clean interfaces has been epitaxially grown, such as graphene/*h*-BN (49), WS_2/WSe_2 (50), and MoS_2/WSe_2 (51). Typically, high-symmetry-stacking configurations with the smallest formation energy are preferably deposited during the vdW epitaxial growth (48, 50). Therefore, it is very challenging to obtain moiré superlattices with on-demand twist angles, especially the metastable samples (e.g., magic-angle TBG) that show strong electron-electron correlation and novel optoelectronic phenomena. Breaking the energy tendency and realizing the scalable fabrication of moiré superlattices with controllable twist angles and layer-by-layer epitaxy would greatly promote the progress of the field.

Dynamic manipulation: For the 'tear-and-stack' technique or vdW epitaxial growth, the final moiré superlattice usually has a fixed twist angle. Therefore, it is often challenging to characterize the twist-angle-dependent behavior. Due to the superlubricity of vdW interfaces, moiré superlattices with dynamically controllable twist angles can be obtained through mechanical, optical, thermal, and magnetic manipulation (52-56). This enables the feasibility to uncover the intrinsic twist-angle-dependent properties. For example, with the atomic force microscope tip manipulation technique, the twist-angle driven evolution of electronic, optical, and mechanical responses in graphene/*h*-BN moiré superlattices have recently been revealed (53).

Visualization of moiré superlattices

Direct visualization of moiré superlattices is fundamentally valuable for the comprehensive understanding and control over emergent moiré physics. In principle, atomic-resolution techniques, such as scanning tunnelling microscopy (STM) and transmission electron microscopy (TEM), offer the opportunity to directly image various moiré superlattices [e.g., magic-angle TBG (29), twisted bilayer WSe_2 (57), and aligned WS_2/WSe_2 (20, 50)]. Specifically, STM can also probe the magnitude of moiré potential in-situ, offering key insight for understanding the moiré physics. Although STM and TEM are powerful in the visualization of moiré superlattices, the special sample preparation and complex operating environment (e.g., ultra-high vacuum and cryogenic temperature) are not conducive to establishing a clear correlation between the direct imaging of moiré structures and the emerging electrical/optical properties.

Because of the broken symmetry and sizeable strain gradients at domain walls, moiré superlattices can show nonvanishing electromechanical responses and hence be imaged by piezoresponse force microscopy (PFM) (58). In particular, PFM provides a simple, universal technique to visualize various moiré superlattices under room-temperature and atmospheric conditions (58). However, PFM requires direct contact with the active area and thus prevents the use of *h*-BN encapsulation and top gates, which are typically required for most optical/transport measurements. Recent studies demonstrate that channeling modulated secondary electron imaging technique can be used to visualize the fully *h*-BN encapsulated, dual-gated moiré superlattice devices (59). With the help

of this advanced technique, the local moiré structures and the exotic photonic properties have been successfully correlated with each other (59), deepening our understanding. Additionally, moiré superlattices can also be visualized by conductive AFM (60), scanning near-field optical microscopy (SNOM) (61), scanning microwave impedance microscopy (sMIM) (62), scanning Kelvin probe microscopy (SKPM) (63) and hyperspectral Raman imaging (64). Table 1 briefly compares the advantages and disadvantages of different visualization techniques of moiré superlattices.

Moiré photonics

Moiré superlattices with a long-wavelength periodic potential landscape offer opportunities to engineer the elementary excitations and light-matter interaction for fascinating photonic phenomena. In this section, we review the state-of-the-art moiré photonics, which mainly covers moiré neutral/charged excitons, resonantly hybridized excitons, moiré polaritons, moiré phonons, reconstructed collective excitations.

Moiré neutral and charged excitons

Exciton, a Coulomb-bound electron-hole pair, dominates the optical properties of a material and hence underlies the development of emerging photonic/optoelectronic applications (65). Recent studies demonstrate that the moiré superlattices open up new avenues for modulating excitonic quasiparticles in both real and momentum spaces, resulting in quantum-dot-like moiré excitons and Bragg-umklapp moiré excitons, respectively (12).

Quantum-dot-like moiré excitons: From the perspective of real-space, moiré superlattices impose a spatially periodic potential landscape on the excitons (66, 67). Therefore, excitons would likely be trapped at the moiré potential minima (Fig. 2A), forming a lattice of quantum-dot-like moiré excitons, a solid-state analogue of a bosonic quantum gas in an optical lattice interesting for quantum photonics (19, 66). Recently, moiré-trapped quantum-dot-like interlayer excitons (IXs), evidenced as a series of discrete photoluminescence (PL) emission lines with ultra-narrow linewidths (e.g., ~100 μeV), have been demonstrated in $MoSe_2/WSe_2$ heterostructures (Fig. 2B) (19, 68, 69). In particular, the moiré potential minima are located at high-symmetry sites that maintain three-fold rotational symmetry (19, 66, 69). Consequently, moiré-trapped excitons can inherit valley-contrasting properties and exhibit strong circular polarization (Fig. 2B), a feature that distinguishes them from quantum emitters localized by random extrinsic potential (19, 70). In addition, due to the quantum-dot-like confinement, moiré-trapped excitons could provide a platform for single-photon sources and quantum photonics, as demonstrated by the photon correlation experiments (Fig. 2D) (23).

Notably, quantum-dot-like moiré IXs show multiple discrete narrow PL lines at low excitation powers, but transform into a broad emission peak as the excitation power increases (Fig. 2C) (19, 69). This feature can be understood as follows: at low laser powers (e.g., a few nW), the number of the photon-excited IXs are around two orders of magnitude smaller than the number of moiré sites, and thus are trapped at different moiré sites (Fig. 2C), because of the dipolar exciton-exciton interactions (69). Absent disorder, only one PL line is expected as the potential minima in different moiré supercells would be degenerate. However, the ubiquity of inhomogeneity and disorder breaks the degeneracy, leading to spectral isolation of moiré-trapped IXs and a series of PL emission lines (19, 69, 71). As the excitation power increases, more IXs are excited, and thus more moiré trapping sites are populated, resulting in an ensemble band of moiré-trapped IXs with a broad linewidth (Fig. 2C) (69). Note that when the exciton density is high enough, moiré traps would be filled up, and excitons approach the regime of free-particle behavior (19, 72, 73).

Moiré-trapped trions: Upon doping of moiré superlattices, moiré-trapped neutral excitons would interact with the excess charge carriers that are also localized at the moiré sites, forming the moiré charged excitons (i.e., moiré-trapped trions) (74, 75). Recently, moiré-trapped IX trions have been demonstrated in $MoSe_2/WSe_2$ heterostructures (69, 73-75). In these experiments, new sets of quantum-dot-like IX trion emission lines with ultra-narrow linewidths appear about 7 meV below the moiré-trapped neutral excitons upon electrostatic doping (Fig. 2E) (74, 75).

Moiré-trapped trions, because of their charged nature, can couple with the electrons/holes in nearest-neighbor moiré sites via long-range Coulomb interactions. And because the charge carriers are also moiré-trapped, the six nearest-neighbor moiré sites are filled sequentially (Fig. 2F) (74). This creates a discrete repulsive Coulomb interaction between moiré-trapped trions and the charge carriers in nearest-neighbor moiré sites. Consequently, moiré-trapped trions show a staircase-like blueshift of energy (Fig. 2F), providing a non-invasive, local optical technique to characterize the Coulomb interactions and local disorder in moiré superlattices (74). In addition, moiré-trapped trions exhibit unique valley properties. For example, the valley polarization can be switched from large co-circular polarization under electron doping to negligible cross-circular polarization under hole doping (74, 75), and the valley polarization time can reach ~1 μs, three orders of magnitude longer than that of conventional trions in monolayer TMDCs (75, 76). This opens up possibilities for opto-valleytronic applications and emerging nanophotonic devices, such as spin-valley optical transistors and chiral light-emitting diodes.

Bragg-umklapp moiré excitons: From the perspective of momentum-space, Bragg-umklapp scattering off the long-period moiré potential can fold the dark exciton states with momentum $k = k_M$ (where k_M is the moiré reciprocal lattice vectors) into the center of mini Brillouin-zone (mBZ), resulting in the formation of new excitonic minibands with optical activity (Fig. 2G) (12, 22, 67, 77-80). Figure 2H illustrates the WSe_2 A exciton dispersion of aligned WSe_2/WS_2 superlattices and clearly shows three optically active excitons at the mBZ center (I, II, and III) (20, 67). Experimentally, Bragg-umklapp intralayer moiré excitons have been demonstrated by both absorption spectroscopy in WSe_2/WS_2 heterobilayers (Fig. 2I) (20, 43) and PL measurements in $MoSe_2/MoS_2$ heterostructures (81). Notably, the cutting-edge exciton band structure calculations reveal that different intralayer moiré excitons exhibit distinct hallmarks (82). In WSe_2/WS_2 moiré superlattices, the lowest energy moiré resonance I is characterized by a Wannier-type exciton with the tightly correlated electron and hole, while the highest energy moiré exciton peak III is described by an intralayer charge-transfer exciton with spatially separated electron and hole (82). Such distinct characters provide unparalleled insight into the unusual doping responses and magneto-optical responses of moiré excitons (20, 82).

For IX species, Bragg-umklapp moiré exciton transitions have also been uncovered by PL spectra in $MoSe_2/WSe_2$ superlattices (Fig. 2J) (21, 83). Due to the strongly modified exciton centre-of-mass wavefunction in real-space, Bragg-umklapp moiré IX resonances exhibit alternating positive and negative circular polarization. Figure 2K shows the real-space distribution of centre-of-mass wavefunctions for the first three Bragg-umklapp moiré IX resonances of $MoSe_2/WSe_2$ heterostructures, which correspond to *s*-, *p*- and *d*-wave symmetry, respectively (21, 79). Because of an additional angular momentum $\hbar$ ($2\hbar$), Bragg-umklapp moiré IX with the *p*-waveform (*d*-waveform) has the opposite (same) optical selection rule as the first *s*-wave symmetry one, leading to alternating co- and cross-circularly polarized PL (21).

Note that in the presence of itinerant electrons/holes, Bragg-umklapp moiré trions can appear in moiré superlattices (84). Besides excitons and trions, Bragg-umklapp scattering off the moiré potential can also activate other elementary excitations, such as phonons, magnons and polaritons.

For example, Bragg-umklapp moiré phonons have been uncovered in TBG (85, 86), graphene/*h*-BN superlattices (86, 87), and twisted bilayer TMDCs (64, 88).

We remark that quantum-dot-like moiré excitons from the real-space perspective and Bragg-umklapp moiré excitons from the momentum-space perspective should be unified in principle. For instance, theoretical calculations show that for the first few Bragg-umklapp moiré excitons with low energy, they are localized at the moiré potential minima and thus should also belong to the quantum-dot-like moiré states (21, 78, 79). Alternatively, for quantum-dot-like moiré excitons observed under ultra-low excitation power, they should correspond to the Bragg-umklapp moiré excitons with the lowest energy. However, for quantum-dot-like moiré excitons and Bragg-umklapp moiré excitons demonstrated by current experimental measurements, they seem to exhibit distinctly different behaviors. For example, the linewidths of Bragg-umklapp moiré excitons are more than two orders of magnitude wider than those of quantum-dot-like moiré excitons. These discrepancies may stem from the ubiquity of disorder/strain/twist-angle inhomogeneity in actual real-world moiré superlattices and deserve further studies to establish a unified understanding.

Resonantly hybridized excitons

Usually, the effects of moiré superlattice on excitons are regarded as a harmonic perturbation potential, then the intralayer excitons and IXs are discussed separately as independent objects (such as the previous section) (66, 67). Such a view holds true for moiré superlattices with large band-edge offset. On the contrary, when the conduction and/or valence band edges of the constituent layers are aligned in both momentum and energy, the resonant interlayer hybridization can strongly enhance the moiré superlattice effects and mix the intralayer excitons and IXs through spin-conserving interlayer hopping, resulting in the resonantly hybridized excitons (12, 22, 89). Resonantly hybridized excitons combine the merits of both intralayer excitons (e.g., large oscillator strength) and IXs (e.g., appreciable out-of-plane dipole moment), and thus represent an advantageous scenario for nanophotonic and optoelectronic applications (90, 91). Resonantly hybridized excitons have been demonstrated in TMDC homobilayer moiré superlattices with intrinsically aligned band edges (40, 89, 92-94), $MoSe_2/WS_2$ moiré heterostructures with nearly degenerate conduction-band edges (Fig. 3A, right panel) (22, 89-91), and WSe_2/WS_2 moiré superlattices where the upper valence band of WS_2 and the lower valence band of WSe_2 are closely aligned (Fig. 3A, left panel) (91). Furthermore, according to the available electron band parameters in the literature (95), we envision that resonantly hybridized excitons can also appear in MoS_2/WS_2, $MoSe_2/WSe_2$, $MoSe_2/MoTe_2$, $MoTe_2/WS_2$, and $MoTe_2/WSe_2$ moiré superlattices.

Interestingly, resonantly hybridized excitons display a sharp energy modulation against the twist angle (Fig. 3B) (22, 89, 90) and manifest energy-level anticrossing under the applied electric fields (Fig. 3C) (89, 91, 92). It is instructive to understand these features using a two-level coupled-oscillator model with Hamiltonian $\begin{pmatrix} \varepsilon_X & \Omega \\ \Omega & \varepsilon_{IX} \end{pmatrix}$, where the off-diagonal element Ω denotes the coupling constant and the diagonal elements ε_X (ε_{IX}) describe the energy of uncoupled intralayer exciton (IX). Because the band minimum of IX is located at the corners of mBZ, IXs that can hybridize with optically bright intralayer excitons should have energy $\varepsilon_{IX} = \varepsilon_{min} + \frac{\hbar^2 \boldsymbol{q}^2}{2M_{IX}}$, where M_{IX} is the total mass of IX, ε_{min} is the IX energy at band minimum and $\boldsymbol{q}$ denotes the momentum of mBZ corners (22, 79, 89, 90). Given that $\boldsymbol{q}$ increases linearly with twist angle, ε_{IX} and hence resonantly hybridized excitons exhibit a sharp energy modulation (Fig. 3B) (22, 89, 90). Meanwhile, IX shows a linear energy shift with applied electric fields due to the quantum-confined Stark effect, leading to the electrically tunable resonantly hybridized excitons (91, 96, 97). When

the energy of IX is tuned to resonate with ε_X, resonantly hybridized excitons would show avoided crossing of the energy-level, as demonstrated by absorption and PL spectra (Fig. 3C) (91, 92). For WSe_2/WS_2 moiré superlattices, the extracted coupling constants Ω can reach ~40 meV, much larger than the exciton linewidths (~10 meV). This indicates that the system is in the exciting strong-coupling regime and provides opportunities for engineering various emerging many-body states, such as Bose-Einstein condensation and polariton superfluidity (91, 98).

Moiré polaritons

Polaritons, a hybrid quasiparticle excitation of part-light and part-matter, enable the fine control of light at the nanoscale across a broad spectral range, promising the prospect of novel technological applications in nanophotonics and optoelectronics (99, 100). Recent studies show that moiré superlattices offer an opportunity for polariton engineering and photonic quantum technologies. Here, we provide an overview of the state-of-the-art moiré exciton-, plasmon-, and phonon-polaritons.

Moiré exciton-polaritons: Because of appreciable oscillator strengths and in-built electric dipoles, resonantly hybridized moiré excitons hold great promise for polaritons with quantum nonlinearity and cooperative effects. $MoSe_2/WS_2$ moiré superlattices with the existence of resonantly hybridized moiré excitons are integrated into a microcavity (101). In place of the resonantly hybridized moiré excitons or the bare cavity photons, three new light-matter hybrid modes with anticrossing of the dispersion curve emerge (Fig. 3D) (101). This demonstrates the moiré exciton-polaritons and the effective coupling between resonantly hybridized excitons and cavity photons. Moreover, the coupling strengths Ω (~10 meV) of moiré exciton-polaritons satisfy $\Omega > \frac{(\gamma_X+\gamma_p)}{2}$ (γ_X/γ_p are the linewidths of the resonantly hybridized excitons/cavity mode), indicating the strongly coupled regime of light-matter interactions (98, 101).

Moiré exciton-polaritons exhibit radically different excitation density responses than polaritons formed with the constituent monolayer excitons (Fig. 3E) (101). For example, with increasing excitation density, the moiré exciton-polaritons (monolayer exciton-polaritons) show a strong drop in coupling strength by up to 20% (negligible change in coupling strength), but no measurable exciton energy shift/line-broadening (considerable blueshift and line-broadening). This suggests the strong exciton blockade and suppressed excitation-induced dephasing for moiré exciton-polaritons, and indicates that the resonantly hybridized exciton involved in the polariton formation should be a moiré-trapped 0D-like exciton (101). Benefitting from the moiré quantum confinement effect, moiré exciton-polaritons can show a nonlinearity up to ~6 $\mu eV \cdot \mu m^2$, more than two orders of magnitude larger than typical monolayer TMDC exciton-polaritons (Fig. 3F) (101). Moiré exciton-polaritons uniquely combine strong quantum nonlinearity and large coupling strength, opening a huge swath of possibilities for quantum photonics and optoelectronics.

Moiré plasmon-polaritons: Plasmon-polaritons are coupled excitations of photons and charge carriers that offer the possibility of manipulating and guiding light at subwavelength scales (99, 100). The ability to control plasmon-polaritons is central to modern information and communication technologies, such as subdiffraction imaging, optical sensing, infrared detectors, light-harvesting devices, and electro-optical modulators (99, 100). Moiré superlattices provide a powerful platform for engineering novel plasmon-polaritons because of the interlayer quantum coupling and radically altered electronic structures (e.g., the emergence of flat bands). For example, due to additive contribution from the interband transition between superlattice minibands, plasmon-polaritons in graphene/*h*-BN moiré superlattices show enhanced scattering amplitudes (102). For TBG moiré superlattices, an exotic interband plasmon-polariton mode

originating from the optical transitions between flat minibands is observed, which is radically different from the conventional intraband plasmon in monolayer graphene (103). By using nanostructured surface plasmon resonators, two new plasmon modes are identified in TBG moiré superlattices: a chiral Berry plasmon mode from uncompensated Berry flux, and a slow plasmon mode from interband transitions between nested subbands (104). In particular, because of the non-trivial Berry curvature, the chiral plasmon mode can show the magnetic-field-free Faraday effect with a polarization rotation of ~15° (Fig. 3G) (104). Such a large Faraday rotation angle is comparable to the conventional Faraday effect accessible by a static magnetic field of 7 T, highlighting the great potential of magnetic-field-free Faraday rotators (104). The slow plasmon mode is within the highly sought-after mid-wave infrared spectral window and would open up opportunities for novel photonic devices, such as infrared devices without fundamental damping and phonon scattering processes (104). It is noteworthy that numerous plasmon-polaritons, such as intrinsically undamped plasmon modes (105), quasi-flat plasmonic bands (106), and plasmonic Dirac cone (107), have been predicted in moiré superlattices and deserve further explorations.

Moiré phonon-polaritons: Phonon-polaritons, collective oscillations that result from the hybridization of photons and optical phonons in polar crystals, can endow a wealth of valuable applications, such as nanoscale light propagation, ultramicroscopy and coherent thermal emission (99, 100). Experimental studies have demonstrated that in twisted stacks of vdW crystal α-MoO_3, interlayer twist angle enables fine control of the dispersion of phonon-polaritons and therefore triggers a topological transition from hyperbolic (open) to elliptical (closed) wavefront geometries (Fig. 3H) (108, 109). Such a transition is determined by a topological quantity and becomes resilient to perturbations, impurities or disorder. When the topological number is two (four), the dispersion of phonon-polaritons is hyperbolic (elliptical) (108, 109). At the twist angle at which the topological transition occurs (dubbed as photonic magic angles), the dispersion becomes flattened, supporting highly collimated, directive and diffractionless canalized phonon-polaritons for various applications, such as quantum nanophotonics, superlens, nanoimaging, biosensing and radiative energy transfer (108).

Photonics of moiré correlated electronic states

Moiré superlattices with enhanced electron-electron correlations in the flat minibands, provide opportunities for a large portfolio of correlated electronic states, such as Mott insulators, Wigner crystal states, charge density waves, charge-transfer insulators and exciton insulators (11, 27, 28, 110-113). For example, nearly two dozen correlated insulating states have been unveiled at the commensurate filling fractions of WSe_2/WS_2 moiré superlattices via an optical sensing technique (Fig. 4A) (11). Certainly, these moiré correlated electronic states would have profound effects on the elementary optical excitations, resulting in a number of photonic responses.

First, due to the gapped nature of moiré correlated electronic states, free carrier screening of the exciton interactions is largely quenched. This would result in the enhancement of oscillator strength and the blueshift of exciton resonance energy for photonics (Fig. 4B) (30, 114, 115). Second, moiré correlated electronic states at commensurate fractional fillings belong to charge-ordered states, e.g., Wigner crystals and charge density waves. Consequently, there is an additional periodic potential for collective excitations, which can fold dark states back to the light cone by Bragg-umklapp scattering and thus brighten new optical transitions (Fig. 4C) (80, 116). Third, for moiré correlated electronic states at some specific fillings (e.g., $\nu = \pm\frac{1}{2}, \pm\frac{3}{5}$), electrons are arranged in alternating lines with a preferential orientation along the high-symmetry axes of the moiré superlattice (11, 30, 112). Such stripe nature of these moiré correlated electronic states

spontaneously breaks the three-fold rotational symmetry, enabling the anisotropic optical responses (30, 117). Last but not least, moiré correlated electronic states can facilitate a wide range of magneto-optical phenomena, such as strongly enhanced valley Zeeman splitting, magnetic circular dichroism, Faraday effect, and Kerr rotation (43, 118, 119). For example, a nearly two orders of magnitude enhanced exciton valley Landé g-factor has been observed for moiré correlated electronic states at $\nu = -1$ (Fig. 4D), opening up possibilities for opto-valleytronic applications (43, 118). By optically tuning the spin exchange interactions between moiré-trapped holes, ferromagnetic order emerges at $\nu = -\frac{1}{3}$ Wigner state of WSe_2/WS_2 moiré superlattice, giving rise to the exotic magnetic circular dichroism (Fig. 4E) (120). Additionally, giant Kerr rotations, over an order of magnitude larger than those observed in typical materials, are predicted in moiré correlated electronic states (119). Nevertheless, coupling strongly correlated electronic states in moiré superlattices with light provides an exciting platform to create, probe and manipulate strongly correlated states and novel light-matter hybrids (e.g., photon-mediated superconductivity/ferroelectricity/ferromagnetism, optically driven topological phenomena, highly correlated light-matter states, and optical spin Hall effect).

Reconstructed collective excitations

In the prior discussion, the influence of moiré superlattices on optical properties is mainly based on a rigid lattice model (left panel, Fig. 4F). By contrast, for moiré superlattices with a large period, the interlayer vdW interaction can compete with the intralayer lattice distortion and favor interlayer commensurability to minimize the misalignment energy, resulting in lattice reconstruction and thus breaking down the rigid lattice picture (60, 121, 122). For instance, a tessellated pattern of AB/BA triangular domains, separated by a network of narrow strain solitons, is formed in marginally twisted graphene and TMDC homobilayers (right panel of Fig. 4F) (60, 121, 122). Undoubtedly, the reconstructed moiré superlattices would cause renormalization of the electronic and optical properties. It was reported that the domain-wall solitons of marginally TBG are topologically protected chiral states and can strongly reflect the plasmon-polaritons (Fig. 4G) (61, 123). Consequently, a regular pattern of plasmon-polaron scatterers with a periodicity close to the wavelength of plasmon-polariton is formed, endowing the TBG moiré superlattice a natural nano-light photonic crystal (61). Crucially, such moiré photonic crystals are lithography-free and electrically tunable, representing an advantageous scenario for optical and optoelectronic telecommunications, as well as controllable quantum optical circuits.

In addition, the domain-wall solitons and soliton interceptions have considerable strain, facilitating strain-engineered photonics. For example, the emergence of strain in reconstructed graphene or MoS_2 moiré superlattices distorts the hexagonal unit cell, leading to the splitting of the doubly-degenerate E_{2g} phonon mode (Fig. 4H) (124, 125). The reconstructed moiré superlattices also have profound impacts on symmetry-breaking photonics. For near-0°-twist-angle TMDC homobilayers, atomic reconstruction leads to the formation of energetically favorable AB and BA stacking. Due to the simultaneous breaking of inversion and mirror symmetries, rhombohedral AB and BA stacking configurations show out-of-plane ferroelectric polarization, but with opposite signs. Therefore, the layer symmetry in reconstructed TMDC moiré superlattices is broken, enabling the emergence of two spatially alternating exciton species with distinct gate tunability and valley coherence properties (Figs. 4I-K) (40, 59). In addition, reconstructed TMDC moiré superlattices open up new avenues to realize tunable exciton arrays and 1D localized exciton states with electrons and holes residing at opposite sides of the domain-wall solitons for applications such as quantum optoelectronics (59).

Moiré optoelectronics

Optoelectronics involves the study and applications of electronic devices that can generate, modulate, detect, interact with or control light, including photodetectors, light-emitting diodes, photovoltaics, modulators, and so on. Moiré superlattices with combined unique electronic and optical properties point to new avenues for cutting-edge optoelectronic applications. In this section, we briefly review the recent developments in state-of-the-art moiré optoelectronics.

Strong mid-/far-infrared photoresponses

In general, moiré superlattices are expected to show strong light-matter interaction and large photoresponses. First, the formation of flat minibands with a large density of states can enhance the dynamical conductivity. Second, the emergence of superlattice bandgap and correlated insulating gap in the order of tens of millielectronvolts can lead to resonance interband transition and thus favor strong photoresponses in the long-sought mid-/far-infrared and even terahertz ranges. When the Fermi level lies in the superlattice bandgap (Fig. 5A), the interband transition between the top of the moiré Dirac band and the bottom of the empty band leads to the resonance-enhanced dynamical conductivity and hence strong mid-infrared photoresponses in TBG moiré superlattices (Fig. 5B) (126). A giant extrinsic photoresponsivity of ~26 mA W^{-1} at the mid-infrared wavelength of 12 μm is achieved in 1.81° TBG, which is almost a factor of 20 larger than the photoresponsivity of natural bilayer graphene (<1.5 mA W^{-1}) (126). As a result, TBG moiré superlattices provide an attractive material platform for the long-sought-after mid-infrared optoelectronic devices.

By using the optical transition between moiré flat minibands, strong far-infrared photocurrent responses have been seen in ABC trilayer graphene/*h*-BN moiré superlattices (Fig. 5C) (127). Due to the electrically tunable moiré minibands, including both the bandwidth and bandgap, the photocurrent responses show high tunability over 80 meV in external electric fields (inset of Fig. 5C) (127). Upon doping the flat moiré miniband to form correlated insulating states, optical transition across the emerging Mott gap can largely enhance the dynamical conductivity and result in strong far-infrared photoresponses. For example, large photoresponses centered at ~18 meV are recently demonstrated at $\nu = \pm 1/2$ Hubbard-Mott insulating states of ABC trilayer graphene/*h*-BN moiré superlattices (Fig. 5D) (127, 128). We highlight that the strong far-infrared photocurrent responses induced by a correlated insulating gap in moiré superlattices can favor exotic optoelectronics and technological advances (e.g., detectors, sensors and modulators).

Symmetry breaking optoelectronics

Moiré superlattices with strong electron correlations usually display various symmetry breaking [e.g., broken inversion symmetry, broken time-reversal symmetry, and broken U(1) gauge symmetry] and thus provide a powerful platform for symmetry-breaking optoelectronics, such as bulk photovoltaic effect (BPVE), opto-valley Hall effects, and chiral light-emitting diode (3, 34, 129). For example, it was shown that because of moiré-induced symmetry breaking and quantum geometrical properties, strong BPVE at ~5 and 7.7 μm can occur in twisted double bilayer graphene moiré superlattices (Fig. 5E) (33). The moiré quantum geometry strongly depends on the displacement field and Fermi level, resulting in electrically tunable BPVE (e.g., the photovoltage amplitude and phase) in twisted double bilayer graphene superlattices. In addition, the mid-infrared BPVE in twisted double bilayer graphene is surprisingly strong and reaches ~3.7 V W^{-1} at 7.7 μm, much larger than previous demonstrations (33). We envision that the ultrastrong mid-infrared BPVE in moiré superlattices will stimulate next-generation applications in nonlinear

optics and optoelectronics, such as intense terahertz sources, biological sensing, energy harvesting, and all-optical transistors.

The gate-tunable BPVE in twisted double bilayer graphene moiré superlattices, together with its dependence on incident optical polarization states, power, and wavelength, provides the possibility for the simultaneous decipherment of full-Stokes polarimetry and wavelength. Indeed, utilizing the tunable mid-infrared BPVE in twisted double bilayer graphene as an encoder and a trained convolutional neural network as a decoder (Fig. 5F), a compact intelligent infrared sensor with merely a subwavelength footprint is achieved (33). After proper training of the convolutional neural network, the intelligent infrared sensing can be well capable of identifying the fingerprint of light, including the full Stokes parameters and the wavelength (Fig. 5G) (33), a pathway for future intelligent sensing technologies in an extremely compact, on-chip manner.

Apart from the mid-infrared BPVE in twisted double bilayer graphene (33), it was also shown that the symmetry of TBG close to the second magic angle (~0.6°) is reduced to point group C_1, breaking both the inversion and rotational symmetries, and enabling the exotic BPVE in the terahertz region (130). It is expected that highly tunable BPVE can also emerge in other moiré superlattices and is worthwhile to explore, especially for rotationally aligned graphene/*h*-BN, hetero- and homo-TMDC bilayers, in which electron correlation-triggered symmetry breaking and giant second-order nonlinear responses have recently been uncovered by electrical-transport (131, 132).

Single-photon detection

The detection of light at the single-photon level is crucial for a host of theoretical, experimental, and technological advances, such as quantum information processing, quantum sensing, quantum key distribution, and radio astronomy (70). By employing heat-induced breaking of the superconducting states in nanostructured superconductors, advanced single-photon detectors with operation wavelengths in the range between visible and near-infrared have been well developed and even commercialized. However, because of high electron density and thus large heat capacity in traditional superconductors, single-photon detector technologies in the ultralow photon energy regions (e.g., mid-infrared and terahertz frequencies) are extremely difficult to achieve. Strikingly, magic-angle TBG moiré superlattices can show dome-shaped superconducting states at a record-low electron density (~10^{12} cm^{-2}), and thus, an extremely small heat capacity (e.g., a few hundred k_B) (Fig. 5H) (133, 134). Consequently, a single photon, even with ultralow energy, can cause a sizable temperature increase to break down the superconducting state, offering extraordinary opportunities for single-photon detection in previously unattainable mid-infrared and even terahertz range (Fig. 5I) (17, 133, 134). Indeed, by quantifying the calorimetric photoresponses, it was demonstrated theoretically that magic-angle TBG can have an ultrabroad detection range of light at the single-photon level from the visible to sub-terahertz with a remarkably fast response time of ~4 ns as well as a high energy resolution better than 1 THz (134). Further efforts are required to experimentally demonstrate such exciting single-photon devices.

In close resemblance to reconstructed photonics, moiré superlattices with lattice reconstruction would also lead to the renormalization of optoelectronic properties, such as the formation of photocurrent patterns (Fig. 5J) (135, 136). In addition, by integrating moiré superlattices with other structures, such as waveguides, cavities, plasmonics, and ring resonator, a large portfolio of fascinating optoelectronic devices with superior performance would emerge, e.g., single photon light-emitting devices, optical modulators, photoinduced valley currents, etc.

Perspectives and conclusions

The field of moiré photonics and optoelectronics is progressing rapidly. A delightful series of moiré photonic/optoelectronic phenomena have been witnessed in the span of less than five years, including but not limited to moiré excitons/polaritons, resonantly hybridized excitons, reconstructed collective excitations, strong mid-infrared photoresponses, intelligent light sensors, and terahertz single-photon detection. This not only opens up exciting possibilities for a wide range of new frontiers in basic scientific research, but also outlines a bright vision for various sophisticated physical phenomena and emerging technological innovations. More significantly, the dizzying pace of recent achievements suggests that we have only seen the tip of the iceberg, and there will be many more surprises to come in moiré photonics and optoelectronics.

Advanced scanning probe techniques

One future direction is to develop new, advanced scanning probe techniques with an ultrahigh spatial resolution (e.g., <5 nm), and therefore can probe the photonic and optoelectronic properties in an individual moiré supercell. Currently, the measurements of moiré photonics/optoelectronics are based on far-field techniques with a spot size of ~1 μm. As a consequence, the detected results are a collection of signals from more than 10,000 moiré unit cells. Due to the ubiquity of twist-angle inhomogeneity and strain from the fabrication of devices, the observed results are often super complex and lack reproducibility. For instance, some moiré photonic/optoelectronic phenomena have been reported by only a single group and are yet to be reproduced by others. Developing new techniques that can locally probe the photonic and optoelectronic properties of different high-symmetry points within a single moiré unit cell [such as four-dimensional scanning TEM spectroscopy technique (137) and near-field scanning technique (61)], will undoubtedly advance our understanding of the current conundrums/contradictions and greatly facilitate the further development of moiré photonics and optoelectronics.

New moiré systems

Considering that there are thousands of 2D crystals and the current research on moiré photonics and optoelectronics is just focused on twisted graphene and twisted TMDCs, one of the particularly intriguing directions is to explore the exotic photonic and optoelectronic phenomena of new moiré systems, such as those moiré superlattices composed of 2D ferroelectric, magnetic, and multiferroic crystals. In particular, recent studies reveal that magnetic moiré superlattices can display a pattern of nanoscale domains that alternate with layered antiferromagnetic and ferromagnetic states (41, 42). Consequently, magnetic moiré superlattices enable the control of magnetic order, symmetry breaking, and interlayer hybridization on the nanoscale (138), opening a huge swath of possibilities for engineering photonic and optoelectronic properties, for example, nonreciprocal second-harmonic generation (139), magnon-exciton coupling (140), and inelastic light scattering (141). Beyond the single moiré, moiré landscape involving two or multiple single moiré superlattices provides another direction and has the potential to spark the next "gold rush" of novel moiré photonics and optoelectronics. For instance, the long-sought boson exciton crystals have been recently evidenced in a $WSe_2/MoSe_2/WSe_2$ heterotrilayer consisting of two single moiré patterns, paving a way towards the exploration of quantum optoelectronics and quantum coherent phenomena (32). Further, moiré superlattices beyond 2D materials, such as 1D vdW moiré superlattices (142), and moiré artificial metamaterials (143, 144), could also offer promising avenues for engineering moiré photonics and optoelectronics, e.g., localization-to-delocalization transition of light (143), magic-angle lasers (144), and optical solitons (145).

Engineering moiré photonics and optoelectronics

Another crucial direction is to control moiré photonic and optoelectronic properties through different external degrees of freedom (such as ultrafast optical excitations, electric/magnetic field, strain, twist angle, doping, pressure, and Floquet engineering). For instance, it has been theoretically elucidated that because of different local static dipole moments, the electric field can switch the global moiré potential minima from one high-symmetry point to another high-symmetry point via quantum-confined Stark effect, enabling the possibilities to program the spatial locations and optical selection rule of moiré-trapped excitons on demand (66). Experimentally, it has also been demonstrated that strain can play a role in tailoring the moiré potential landscape and optoelectronic response (146). To name a few, uniaxial strain can tune the array of quantum dot-like 0D traps into parallel stripes of 1D quantum wires, breaking the three-fold rotational symmetry and changing the optical selection rule of moiré exciton from circular to linear (146). It was shown that the itinerant excitons excited by light can highly tune the spin-spin exchange interactions between moiré-trapped carriers and result in ferromagnetic order in WS_2/WSe_2 moiré superlattices, outlining the possibility of all-optical control of emergent moiré photonic and optoelectronic phenomena (120).

Novel technical innovations

Particularly interesting fields where moiré optoelectronics have the potential to trigger new on-chip applications include, but not limited to, high-performance moiré lasers, quantum simulation of Bose-Hubbard model and programmable quantum light sources. Recently, by integrating MoS_2/WSe_2 superlattices with a silicon topological nanocavity, ultra-low-threshold broadband excitonic lasing at the technologically important telecommunication O-band (1260-1360 nm) has been achieved at room temperature (147). The moiré excitonic laser shows the highest spectral coherence of < 0.1 nm linewidth among all 2D material-based laser systems studied so far, facilitating high-performance on-chip photonics and optoelectronics (e.g., electrically-pumped wavelength-tunable moiré lasers) (147). Further, due to enhanced Coulomb interactions, moiré superlattices offer opportunities to create a regular array of spatially ordered quantum emitters. In the case of moiré interlayer excitons with long lifetime and strong dipolar interactions, the perfect arrays provide a promising paradigm for the realization of quantum simulation of Bose-Hubbard model. It is noteworthy that the Bose-Hubbard model, which underlies rich bosonic states of matter and quantum phase transitions, is challenging to achieve in solid-state systems. Theoretically, a wide variety of bosonic quantum matter phases and quantum phase transition associated with quantum-dot-like interlayer excitons have been predicted in moiré superlattices, such as exciton supersolid, superfluid-insulator phase transition, and bosonic Mott insulator (148, 149). Experimentally, exciton Mott insulator and exciton density waves have been recently reported in WSe_2/WS_2 and coulomb-coupled WS_2/bilayer WSe_2/WS_2 dual moiré superlattices, respectively (150, 151).

In addition, in the case of intralayer excitons with high quantum efficiency and relatively low sensitivity to disorder in the surrounding dielectric, the spatially ordered moiré exciton array could serve as a super-bright quantum light source (12, 66). In particular, moiré quantum light sources show high programmability with polarization configuration and wavelength controlled by optical pumping, electric field, and strain. Such programmable quantum light sources would provide a firm basis for the exploration of coherent quantum phenomena of optical bosons and the development of various quantum technologies (70), such as the generation of polarization-entangled photon pairs, Dicke superradiance, spin-photon interfaces, quantum information processing, encryption, and sensing. In addition, moiré superlattices, by integrating with other optical systems (e.g., optical cavities, resonances, silicon-based waveguides, and fibers), will

undoubtedly outline a bright vision for numerous emerging photonic and optoelectronic applications, such as quantum nonlinear optics, lasers, imaging arrays, modulators/switches, and polarization devices.

References and Notes

1. K. Novoselov, A. Mishchenko, A. Carvalho, A. C. Neto, 2D materials and van der Waals heterostructures. *Science* **353**, aac9439 (2016).
2. C. Jin *et al.*, Ultrafast dynamics in van der Waals heterostructures. *Nat. Nanotechnol.* **13**, 994-1003 (2018).
3. L. Du *et al.*, Engineering symmetry breaking in 2D layered materials. *Nat. Rev. Phys.* **3**, 193-206 (2021).
4. B. Huang *et al.*, Emergent phenomena and proximity effects in two-dimensional magnets and heterostructures. *Nat. Mater.* **19**, 1276-1289 (2020).
5. N. Briggs *et al.*, Atomically thin half-van der Waals metals enabled by confinement heteroepitaxy. *Nat. Mater.* **19**, 637-643 (2020).
6. Q. H. Wang, K. Kalantar-Zadeh, A. Kis, J. N. Coleman, M. S. Strano, Electronics and optoelectronics of two-dimensional transition metal dichalcogenides. *Nat. Nanotechnol.* **7**, 699-712 (2012).
7. L. Du *et al.*, 2D proximate quantum spin liquid state in atomic-thin α-$RuCl_3$. *2D Mater.* **6**, 015014 (2018).
8. A. K. Geim, I. V. Grigorieva, Van der Waals heterostructures. *Nature* **499**, 419-425 (2013).
9. Y. Liu *et al.*, Van der Waals heterostructures and devices. *Nat. Rev. Mater.* **1**, 16042 (2016).
10. E. Y. Andrei *et al.*, The marvels of moiré materials. *Nat. Rev. Mater.* **6**, 201-206 (2021).
11. Y. Xu *et al.*, Correlated insulating states at fractional fillings of moiré superlattices. *Nature* **587**, 214-218 (2020).
12. N. P. Wilson, W. Yao, J. Shan, X. Xu, Excitons and emergent quantum phenomena in stacked 2D semiconductors. *Nature* **599**, 383-392 (2021).
13. K. F. Mak, J. Shan, Semiconductor moiré materials. *Nat. Nanotechnol.* **17**, 686-695 (2022).
14. R. Bistritzer, A. H. MacDonald, Moiré bands in twisted double-layer graphene. *Proc. Natl Acad. Sci. USA* **108**, 12233-12237 (2011).
15. L. A. Ponomarenko *et al.*, Cloning of Dirac fermions in graphene superlattices. *Nature* **497**, 594-597 (2013).
16. C. R. Dean *et al.*, Hofstadter's butterfly and the fractal quantum Hall effect in moiré superlattices. *Nature* **497**, 598-602 (2013).
17. Y. Cao *et al.*, Unconventional superconductivity in magic-angle graphene superlattices. *Nature* **556**, 43-50 (2018).
18. Y. Cao *et al.*, Correlated insulator behaviour at half-filling in magic-angle graphene superlattices. *Nature* **556**, 80-84 (2018).
19. K. L. Seyler *et al.*, Signatures of moiré-trapped valley excitons in $MoSe_2/WSe_2$ heterobilayers. *Nature* **567**, 66-70 (2019).
20. C. Jin *et al.*, Observation of moiré excitons in WSe_2/WS_2 heterostructure superlattices. *Nature* **567**, 76-80 (2019).
21. K. Tran *et al.*, Evidence for moiré excitons in van der Waals heterostructures. *Nature* **567**, 71-75 (2019).
22. E. M. Alexeev *et al.*, Resonantly hybridized excitons in moiré superlattices in van der Waals heterostructures. *Nature* **567**, 81-86 (2019).
23. H. Baek *et al.*, Highly energy-tunable quantum light from moiré-trapped excitons. *Sci. Adv.* **6**, eaba8526 (2020).

24. A. L. Sharpe *et al.*, Emergent ferromagnetism near three-quarters filling in twisted bilayer graphene. *Science* **365**, 605-608 (2019).
25. G. Chen *et al.*, Tunable correlated Chern insulator and ferromagnetism in a moiré superlattice. *Nature* **579**, 56-61 (2020).
26. M. Serlin *et al.*, Intrinsic quantized anomalous Hall effect in a moiré heterostructure. *Science* **367**, 900-903 (2020).
27. E. C. Regan *et al.*, Mott and generalized Wigner crystal states in WSe_2/WS_2 moiré superlattices. *Nature* **579**, 359-363 (2020).
28. X. Huang *et al.*, Correlated insulating states at fractional fillings of the WS_2/WSe_2 moiré lattice. *Nat. Phys.* **17**, 715-719 (2021).
29. Y. Jiang *et al.*, Charge order and broken rotational symmetry in magic-angle twisted bilayer graphene. *Nature* **573**, 91-95 (2019).
30. C. Jin *et al.*, Stripe phases in WSe_2/WS_2 moiré superlattices. *Nat. Mater.* **20**, 940-944 (2021).
31. M. Haavisto, J. Lado, A. O. Fumega, Topological multiferroic order in twisted transition metal dichalcogenide bilayers. *SciPost Phys.* 13, 052 (2022).
32. Y. Bai *et al.*, Evidence for Exciton Crystals in a 2D Semiconductor Heterotrilayer. *arXiv:2207.09601* (2022).
33. C. Ma *et al.*, Intelligent infrared sensing enabled by tunable moiré quantum geometry. *Nature* **604**, 266-272 (2022).
34. C. N. Lau, M. W. Bockrath, K. F. Mak, F. Zhang, Reproducibility in the fabrication and physics of moiré materials. *Nature* **602**, 41-50 (2022).
35. D. Huang, J. Choi, C.-K. Shih, X. Li, Excitons in semiconductor moiré superlattices. *Nat. Nanotechnol.* **17**, 227-238 (2022).
36. E. C. Regan *et al.*, Emerging exciton physics in transition metal dichalcogenide heterobilayers. *Nat. Rev. Mater.* **7**, 778-795 (2022).
37. K. Kim *et al.*, van der Waals Heterostructures with High Accuracy Rotational Alignment. *Nano Lett.* **16**, 1989-1995 (2016).
38. R. Frisenda *et al.*, Recent progress in the assembly of nanodevices and van der Waals heterostructures by deterministic placement of 2D materials. *Chem. Soc. Rev.* **47**, 53-68 (2018).
39. L. Wang *et al.*, Correlated electronic phases in twisted bilayer transition metal dichalcogenides. *Nat. Mater.* **19**, 861-866 (2020).
40. J. Sung *et al.*, Broken mirror symmetry in excitonic response of reconstructed domains in twisted $MoSe_2/MoSe_2$ bilayers. *Nat. Nanotechnol.* **15**, 750-754 (2020).
41. T. Song *et al.*, Direct visualization of magnetic domains and moiré; magnetism in twisted 2D magnets. *Science* **374**, 1140-1144 (2021).
42. Y. Xu *et al.*, Coexisting ferromagnetic–antiferromagnetic state in twisted bilayer CrI_3. *Nat. Nanotechnol.* **17**, 143-147 (2022).
43. Y. Tang *et al.*, Simulation of Hubbard model physics in WSe_2/WS_2 moiré superlattices. *Nature* **579**, 353-358 (2020).
44. A. J. Mannix *et al.*, Robotic four-dimensional pixel assembly of van der Waals solids. *Nat. Nanotechnol.* **17**, 361-366 (2022).
45. S. Masubuchi *et al.*, Autonomous robotic searching and assembly of two-dimensional crystals to build van der Waals superlattices. *Nat. Commun.* **9**, 1413 (2018).
46. Q. Wang *et al.*, Layer-by-layer epitaxy of multilayer MoS_2 wafers. *Natl Sci. Rev.* **9**, nwac077 (2022).
47. P. Solís-Fernández, H. Ago, Machine Learning Determination of the Twist Angle of Bilayer

Graphene by Raman Spectroscopy: Implications for van der Waals Heterostructures. *ACS Appl. Nano Mater.* **5**, 1356-1366 (2022).
48. P. Chen, Z. Zhang, X. Duan, X. Duan, Chemical synthesis of two-dimensional atomic crystals, heterostructures and superlattices. *Chem. Soc. Rev.* **47**, 3129-3151 (2018).
49. W. Yang *et al.*, Epitaxial growth of single-domain graphene on hexagonal boron nitride. *Nat. Mater.* **12**, 792-797 (2013).
50. L. Yuan *et al.*, Twist-angle-dependent interlayer exciton diffusion in WS_2-WSe_2 heterobilayers. *Nat. Mater.* **19**, 617-623 (2020).
51. C. Zhang *et al.*, Interlayer couplings, moiré patterns, and 2D electronic superlattices in MoS_2/WSe_2 hetero-bilayers. *Sci. Adv.* **3**, e1601459 (2017).
52. L. Du *et al.*, Modulating PL and electronic structures of MoS_2/graphene heterostructures via interlayer twisting angle. *Appl. Phys. Lett.* **111**, 263106 (2017).
53. R. Ribeiro-Palau *et al.*, Twistable electronics with dynamically rotatable heterostructures. *Science* **361**, 690-693 (2018).
54. M. Liao *et al.*, Ultra-low friction and edge-pinning effect in large-lattice-mismatch van der Waals heterostructures. *Nat. Mater.* **21**, 47-53 (2022).
55. S. T. M. Akkanen, H. A. Fernandez, Z. Sun, Optical Modification of 2D Materials: Methods and Applications. *Adv. Mater.* **34**, 2110152 (2022).
56. D. Wang *et al.*, Thermally Induced Graphene Rotation on Hexagonal Boron Nitride. *Phys. Rev. Lett.* **116**, 126101 (2016).
57. Z. Zhang *et al.*, Flat bands in twisted bilayer transition metal dichalcogenides. *Nat. Phys.* **16**, 1093-1096 (2020).
58. L. J. McGilly *et al.*, Visualization of moiré superlattices. *Nat. Nanotechnol.* **15**, 580-584 (2020).
59. T. I. Andersen *et al.*, Excitons in a reconstructed moiré potential in twisted WSe_2/WSe_2 homobilayers. *Nat. Mater.* **20**, 480-487 (2021).
60. A. Weston *et al.*, Atomic reconstruction in twisted bilayers of transition metal dichalcogenides. *Nat. Nanotechnol.* **15**, 592-597 (2020).
61. S. S. Sunku *et al.*, Photonic crystals for nano-light in moiré graphene superlattices. *Science* **362**, 1153-1156 (2018).
62. K. Lee *et al.*, Ultrahigh-resolution scanning microwave impedance microscopy of moiré lattices and superstructures. *Sci. Adv.* **6**, eabd1919 (2020).
63. J. Yu *et al.*, Imaging Graphene Moiré Superlattices via Scanning Kelvin Probe Microscopy. *Nano Lett.* **21**, 3280-3286 (2021).
64. K.-Q. Lin *et al.*, Large-Scale Mapping of Moiré Superlattices by Hyperspectral Raman Imaging. *Adv. Mater.* **33**, 2008333 (2021).
65. G. Wang *et al.*, Colloquium: Excitons in atomically thin transition metal dichalcogenides. *Rev. Mod. Phys.* **90**, 021001 (2018).
66. H. Yu, G.-B. Liu, J. Tang, X. Xu, W. Yao, Moiré excitons: From programmable quantum emitter arrays to spin-orbit-coupled artificial lattices. *Sci. Adv.* **3**, e1701696 (2017).
67. F. Wu, T. Lovorn, A. H. MacDonald, Topological Exciton Bands in Moiré Heterojunctions. *Phys. Rev. Lett.* **118**, 147401 (2017).
68. M. Brotons-Gisbert *et al.*, Spin-layer locking of interlayer excitons trapped in moiré potentials. *Nat. Mater.* **19**, 630-636 (2020).
69. M. Brotons-Gisbert *et al.*, Moiré-Trapped Interlayer Trions in a Charge-Tunable WSe_2/$MoSe_2$ Heterobilayer. *Phys. Rev. X* **11**, 031033 (2021).
70. M. Turunen *et al.*, Quantum photonics with layered 2D materials. *Nat. Rev. Phys.* **4**, 219-236 (2022).

71. S. Zhao *et al.*, Excitons in mesoscopically reconstructed moiré hetersotructures. *arXiv:*2202.11139 (2022).
72. J. Wang *et al.*, Diffusivity Reveals Three Distinct Phases of Interlayer Excitons in $MoSe_2/WSe_2$ Heterobilayers. *Phys. Rev. Lett.* **126**, 106804 (2021).
73. E. Liu *et al.*, Signatures of moiré trions in $WSe_2/MoSe_2$ heterobilayers. *Nature* **594**, 46-50 (2021).
74. H. Baek *et al.*, Optical read-out of Coulomb staircases in a moiré superlattice via trapped interlayer trions. *Nat. Nanotechnol.* **16**, 1237-1243 (2021).
75. X. Wang *et al.*, Moiré trions in $MoSe_2/WSe_2$ heterobilayers. *Nat. Nanotechnol.* **16**, 1208-1213 (2021).
76. K. F. Mak, D. Xiao, J. Shan, Light-valley interactions in 2D semiconductors. *Nat. Photon.* **12**, 451 (2018).
77. H. Yu, Y. Wang, Q. Tong, X. Xu, W. Yao, Anomalous Light Cones and Valley Optical Selection Rules of Interlayer Excitons in Twisted Heterobilayers. *Phys. Rev. Lett.* **115**, 187002 (2015).
78. S. Brem, C. Linderälv, P. Erhart, E. Malic, Tunable Phases of Moiré Excitons in van der Waals Heterostructures. *Nano Lett.* **20**, 8534-8540 (2020).
79. F. Wu, T. Lovorn, A. H. MacDonald, Theory of optical absorption by interlayer excitons in transition metal dichalcogenide heterobilayers. *Phys. Rev. B* **97**, 035306 (2018).
80. T. Smoleński *et al.*, Signatures of Wigner crystal of electrons in a monolayer semiconductor. *Nature* **595**, 53-57 (2021).
81. N. Zhang *et al.*, Moiré Intralayer Excitons in a $MoSe_2/MoS_2$ Heterostructure. *Nano Lett.* **18**, 7651-7657 (2018).
82. M. H. Naik *et al.*, Intralayer charge-transfer moiré excitons in van der Waals superlattices. *Nature* **609**, 52-57 (2022).
83. A. Ciarrocchi *et al.*, Polarization switching and electrical control of interlayer excitons in two-dimensional van der Waals heterostructures. *Nat. Photon.* **13**, 131-136 (2019).
84. E. Marcellina *et al.*, Evidence for Moiré Trions in Twisted $MoSe_2$ Homobilayers. *Nano Lett.* **21**, 4461-4468 (2021).
85. A. Righi *et al.*, Graphene moiré patterns observed by umklapp double-resonance Raman scattering. *Phys. Rev. B* **84**, 241409 (2011).
86. G. S. N. Eliel *et al.*, Intralayer and interlayer electron-phonon interactions in twisted graphene heterostructures. *Nat. Commun.* **9**, 1221 (2018).
87. A. Eckmann *et al.*, Raman fingerprint of aligned graphene/h-BN superlattices. *Nano Lett.* **13**, 5242-5246 (2013).
88. M. Liao *et al.*, Precise control of the interlayer twist angle in large scale MoS_2 homostructures. *Nat. Commun.* **11**, 2153 (2020).
89. D. A. Ruiz-Tijerina, V. I. Fal'ko, Interlayer hybridization and moiré superlattice minibands for electrons and excitons in heterobilayers of transition-metal dichalcogenides. *Phys. Rev. B* **99**, 125424 (2019).
90. L. Zhang *et al.*, Twist-angle dependence of moiré excitons in $WS_2/MoSe_2$ heterobilayers. *Nat. Commun.* **11**, 5888 (2020).
91. Y. Tang *et al.*, Tuning layer-hybridized moiré excitons by the quantum-confined Stark effect. *Nat. Nanotechnol.* **16**, 52-57 (2021).
92. Y. Shimazaki *et al.*, Strongly correlated electrons and hybrid excitons in a moiré heterostructure. *Nature* **580**, 472-477 (2020).
93. H. Yu, W. Yao, Luminescence Anomaly of Dipolar Valley Excitons in Homobilayer Semiconductor Moiré Superlattices. *Phys. Rev. X* **11**, 021042 (2021).

94. S. Brem *et al.*, Hybridized intervalley moiré excitons and flat bands in twisted WSe_2 bilayers. *Nanoscale* **12**, 11088-11094 (2020).
95. C. Zhang *et al.*, Systematic study of electronic structure and band alignment of monolayer transition metal dichalcogenides in Van der Waals heterostructures. *2D Mater.* **4**, 015026 (2016).
96. P. Rivera *et al.*, Interlayer valley excitons in heterobilayers of transition metal dichalcogenides. *Nat. Nanotechnol.* **13**, 1004-1015 (2018).
97. Y. Zhao *et al.*, Interlayer exciton complexes in bilayer MoS_2. *Phys. Rev. B* **105**, L041411 (2022).
98. C. Schneider, M. M. Glazov, T. Korn, S. Höfling, B. Urbaszek, Two-dimensional semiconductors in the regime of strong light-matter coupling. *Nat. Commun.* **9**, 2695 (2018).
99. D. Basov, M. Fogler, F. G. de Abajo, Polaritons in van der Waals materials. *Science* **354**, aag1992 (2016).
100. T. Low *et al.*, Polaritons in layered two-dimensional materials. *Nat. Mater.* **16**, 182 (2017).
101. L. Zhang *et al.*, Van der Waals heterostructure polaritons with moiré-induced nonlinearity. *Nature* **591**, 61-65 (2021).
102. G. X. Ni *et al.*, Plasmons in graphene moiré superlattices. *Nat. Mater.* **14**, 1217-1222 (2015).
103. N. C. H. Hesp *et al.*, Observation of interband collective excitations in twisted bilayer graphene. *Nat. Phys.* **17**, 1162-1168 (2021).
104. T. Huang *et al.*, Observation of chiral and slow plasmons in twisted bilayer graphene. *Nature* **605**, 63-68 (2022).
105. C. Lewandowski, L. Levitov, Intrinsically undamped plasmon modes in narrow electron bands. *Proc. Natl Acad. Sci. USA* **116**, 20869-20874 (2019).
106. T. Stauber, H. Kohler, Quasi-Flat Plasmonic Bands in Twisted Bilayer Graphene. *Nano Lett.* **16**, 6844-6849 (2016).
107. L. Brey, T. Stauber, T. Slipchenko, L. Martín-Moreno, Plasmonic Dirac Cone in Twisted Bilayer Graphene. *Phys. Rev. Lett.* **125**, 256804 (2020).
108. G. Hu *et al.*, Topological polaritons and photonic magic angles in twisted α-MoO_3 bilayers. *Nature* **582**, 209-213 (2020).
109. M. Chen *et al.*, Configurable phonon polaritons in twisted α-MoO_3. *Nat. Mater.* **19**, 1307-1311 (2020).
110. Z. Zhang *et al.*, Correlated interlayer exciton insulator in heterostructures of monolayer WSe_2 and moiré WS_2/WSe_2. *Nat. Phys.* **18**, 1214-1220 (2022).
111. J. Gu *et al.*, Dipolar excitonic insulator in a moiré lattice. *Nat. Phys.* **18**, 395-400 (2022).
112. H. Li *et al.*, Imaging two-dimensional generalized Wigner crystals. *Nature* **597**, 650-654 (2021).
113. L. Ma *et al.*, Strongly correlated excitonic insulator in atomic double layers. *Nature* **598**, 585-589 (2021).
114. E. Liu *et al.*, Excitonic and Valley-Polarization Signatures of Fractional Correlated Electronic Phases in a WSe_2/WS_2 Moiré Superlattice. *Phys. Rev. Lett.* **127**, 037402 (2021).
115. S. Miao *et al.*, Strong interaction between interlayer excitons and correlated electrons in WSe_2/WS_2 moiré superlattice. *Nat. Commun.* **12**, 3608 (2021).
116. Y. Shimazaki *et al.*, Optical Signatures of Periodic Charge Distribution in a Mott-like Correlated Insulator State. *Phys. Rev. X* **11**, 021027 (2021).
117. L. Du *et al.*, Giant anisotropic photonics in the 1D van der Waals semiconductor fibrous red phosphorus. *Nat. Commun.* **12**, 4822 (2021).
118. A. J. Campbell *et al.*, Exciton-polarons in the presence of strongly correlated electronic

states in a $MoSe_2/WSe_2$ moiré superlattice. *npj 2D Mater. Appl.* 6, 79 (2022).
119. J. Liu, X. Dai, Anomalous Hall effect, magneto-optical properties, and nonlinear optical properties of twisted graphene systems. *npj Computat. Mater.* **6**, 57 (2020).
120. X. Wang *et al.*, Light-induced ferromagnetism in moiré superlattices. *Nature* **604**, 468-473 (2022).
121. H. Yoo *et al.*, Atomic and electronic reconstruction at the van der Waals interface in twisted bilayer graphene. *Nat. Mater.* **18**, 448-453 (2019).
122. V. V. Enaldiev, V. Zólyomi, C. Yelgel, S. J. Magorrian, V. I. Fal'ko, Stacking Domains and Dislocation Networks in Marginally Twisted Bilayers of Transition Metal Dichalcogenides. *Phys. Rev. Lett.* **124**, 206101 (2020).
123. L. Jiang *et al.*, Soliton-dependent plasmon reflection at bilayer graphene domain walls. *Nat. Mater.* **15**, 840-844 (2016).
124. J. Quan *et al.*, Phonon renormalization in reconstructed MoS_2 moiré superlattices. *Nat. Mater.* **20**, 1100-1105 (2021).
125. A. C. Gadelha *et al.*, Localization of lattice dynamics in low-angle twisted bilayer graphene. *Nature* **590**, 405-409 (2021).
126. B. Deng *et al.*, Strong mid-infrared photoresponse in small-twist-angle bilayer graphene. *Nat. Photon.* **14**, 549-553 (2020).
127. J. Yang *et al.*, Spectroscopy signatures of electron correlations in a trilayer graphene/hBN moiré superlattice. *Science* **375**, 1295-1299 (2022).
128. G. Chen *et al.*, Signatures of tunable superconductivity in a trilayer graphene moiré superlattice. *Nature* **572**, 215-219 (2019).
129. Q. Ma, A. G. Grushin, K. S. Burch, Topology and geometry under the nonlinear electromagnetic spotlight. *Nat. Mater.* **20**, 1601-1614 (2021).
130. M. Otteneder *et al.*, Terahertz Photogalvanics in Twisted Bilayer Graphene Close to the Second Magic Angle. *Nano Lett.* **20**, 7152-7158 (2020).
131. P. He *et al.*, Graphene moiré superlattices with giant quantum nonlinearity of chiral Bloch electrons. *Nat. Nanotechnol.* **17**, 378-383 (2022).
132. M. Huang *et al.*, Giant nonlinear Hall effect in twisted bilayer WSe_2. *Natl Sci. Rev.* nwac232, doi.org/10.1093/nsr/nwac232 (2022).
133. X. Lu *et al.*, Superconductors, orbital magnets and correlated states in magic-angle bilayer graphene. *Nature* **574**, 653-657 (2019).
134. P. Seifert *et al.*, Magic-Angle Bilayer Graphene Nanocalorimeters: Toward Broadband, Energy-Resolving Single Photon Detection. *Nano Lett.* **20**, 3459-3464 (2020).
135. S. S. Sunku *et al.*, Hyperbolic enhancement of photocurrent patterns in minimally twisted bilayer graphene. *Nat. Commun.* **12**, 1641 (2021).
136. N. C. H. Hesp *et al.*, Nano-imaging photoresponse in a moiré unit cell of minimally twisted bilayer graphene. *Nat. Commun.* **12**, 1640 (2021).
137. X. Yan *et al.*, Single-defect phonons imaged by electron microscopy. *Nature* **589**, 65-69 (2021).
138. N. P. Wilson *et al.*, Interlayer electronic coupling on demand in a 2D magnetic semiconductor. *Nat. Mater.* **20**, 1657-1662 (2021).
139. Z. Sun *et al.*, Giant nonreciprocal second-harmonic generation from antiferromagnetic bilayer CrI_3. *Nature* **572**, 497-501 (2019).
140. Y. J. Bae *et al.*, Exciton-coupled coherent magnons in a 2D semiconductor. *Nature* **609**, 282-286 (2022).
141. B. Huang *et al.*, Tuning inelastic light scattering via symmetry control in the two-dimensional magnet CrI_3. *Nat. Nanotechnol.* **15**, 212-216 (2020).

142. S. Zhao, R. Kitaura, P. Moon, M. Koshino, F. Wang, Interlayer Interactions in 1D Van der Waals Moiré Superlattices. *Adv. Sci.* **9**, 2103460 (2022).
143. P. Wang *et al.*, Localization and delocalization of light in photonic moiré lattices. *Nature* **577**, 42-46 (2020).
144. X.-R. Mao, Z.-K. Shao, H.-Y. Luan, S.-L. Wang, R.-M. Ma, Magic-angle lasers in nanostructured moiré superlattice. *Nat. Nanotechnol.* **16**, 1099-1105 (2021).
145. Q. Fu *et al.*, Optical soliton formation controlled by angle twisting in photonic moiré lattices. *Nat. Photon.* **14**, 663-668 (2020).
146. Y. Bai *et al.*, Excitons in strain-induced one-dimensional moiré potentials at transition metal dichalcogenide heterojunctions. *Nat. Mater.* **19**, 1068-1073 (2020).
147. Q. Lin *et al.*, A room-temperature moiré interlayer exciton laser. *arXiv:2302.01266* (2023).
148. Y.-H. Zhang, D. N. Sheng, A. Vishwanath, SU(4) Chiral Spin Liquid, Exciton Supersolid, and Electric Detection in Moiré Bilayers. *Phys. Rev. Lett.* **127**, 247701 (2021).
149. Z. Bi, L. Fu, Excitonic density wave and spin-valley superfluid in bilayer transition metal dichalcogenide. *Nat. Commun.* **12**, 642 (2021).
150. R. Xiong *et al.*, Bosonic Mott insulator in WSe_2/WS_2 moiré superlattice. *arXiv:2207.10764* (2022).
151. Y. Zeng *et al.*, Exciton density waves in Coulomb-coupled dual moiré lattices. *Nat. Mater.* **22**, 175-179 (2023).

Acknowledgments

Z.S. thanks J. Bai and Z. Ren for discussion and assistance during his current visiting professorship at Northwestern University, China. **Funding:** The authors gratefully acknowledge the financial support from the National Science Foundation of China (NSFC) (grant Nos. 12274447, 61888102 and 11834017), the National Key Research and Development Program (grant no. 2021YFA1202900), the Strategic Priority Research Program of the Chinese Academy of Sciences (grant no. XDB30000000), and the Key-Area Research and Development Program of Guangdong Province (Grant No. 2020B0101340001), the Academy of Finland (314810, 333982, 336144, 333099, 336818, 352780, 352930, and 353364), the Academy of Finland Flagship Programme (320167, PREIN), ERC (834742), the EU H2020-MSCA-RISE-872049 (IPN-Bio), the European Union's Horizon 2020 research and innovation program (965124, FEMTOCHIP), and the National Science Centre, Poland (grant no. 2018/31/B/ST3/02111). F.W. acknowledges the support from U.S. Department of Energy, Office of Science, Office of Basic Energy Sciences, Materials Sciences and Engineering Division under Contract No. DE-AC02-05-CH11231 (van der Waals heterostructure program KCFW16).

Author contributions: L.D., G.Z and Z.S. conceived the idea and led the writing. M.M., Z.H and F.W. contributed substantially to the discussion of the content. All authors reviewed and edited the manuscript before submission.

Competing interests: The authors declare no competing interests.

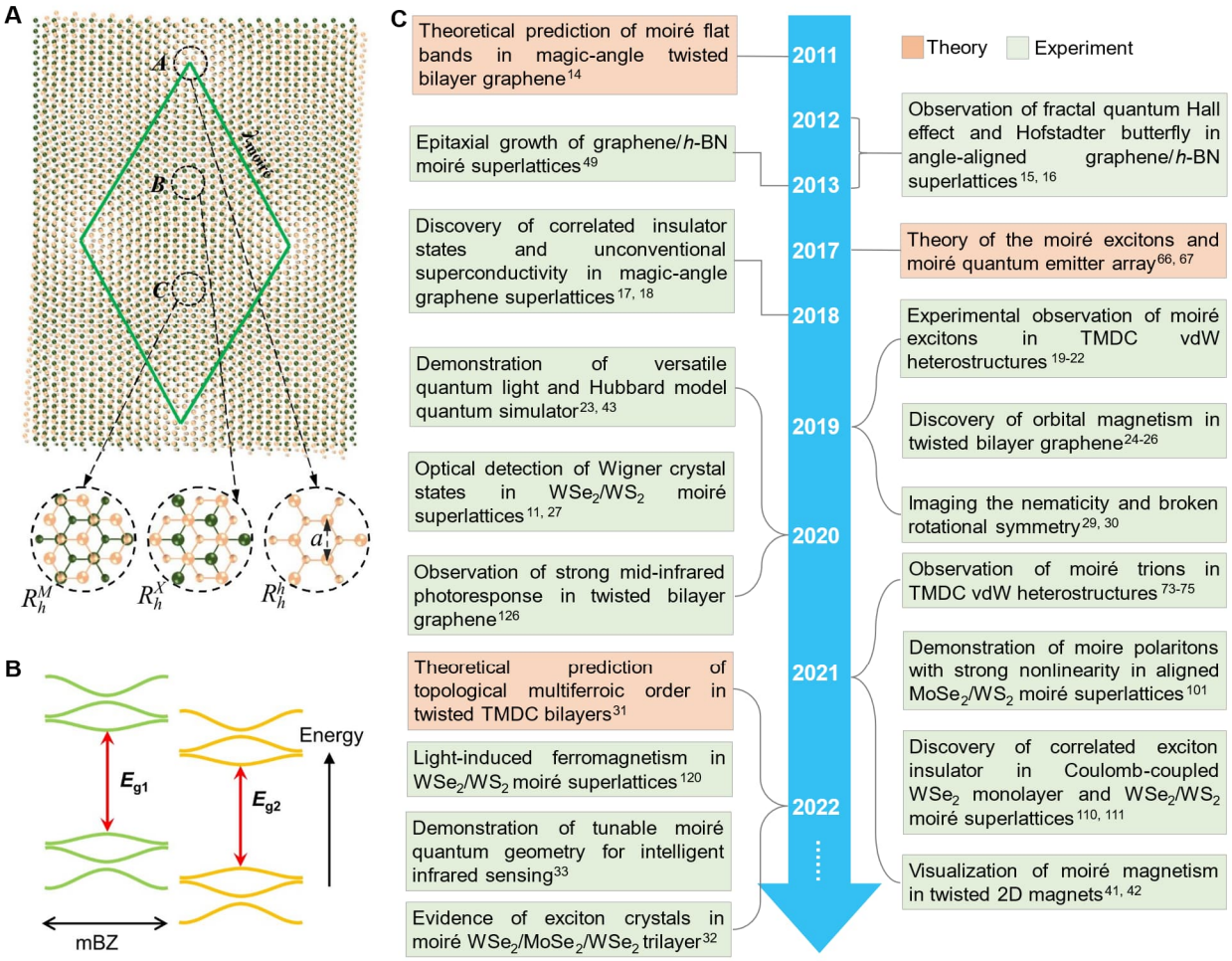

Fig. 1. Moiré superlattices and timeline of key developments in the study of moiré physics. (**A**) Top: illustration of the moiré superlattice formed by a nearly 0-degree angle-aligned TMDC heterobilayer. The moiré unit cell is outlined in the green diamond. Bottom: the close-ups of the three high-symmetry points (A, B and C). Atomic registry R_h^μ denotes an R-type stacking, with the μ site of the top layer vertically aligned with the hexagon center (h) of the bottom layer. (**B**) Schematic of the flat moiré bands in mBZ for moiré heterostructures with type-II band alignment. E_{g1} and E_{g2} stand for the bandgap of the two constituent TMDC layers. (**C**) The timeline of selected key developments in the study of moiré physics. Over the past few years, the field of moiré superlattices has grown substantially and seen a delightful series of new discoveries, such as orbital magnetism, Wigner crystal states, electronic nematic phase, tunable spin-polarized correlated states, simulation of Hubbard model physics, continuous Mott transition, quantum anomalous Hall effect, moiré excitons/polaritons, strong mid-infrared photoresponse, light-induced ferromagnetism and highly tunable bulk photogalvanic effects. Adapted with permission from: **a**, Ref.(66).

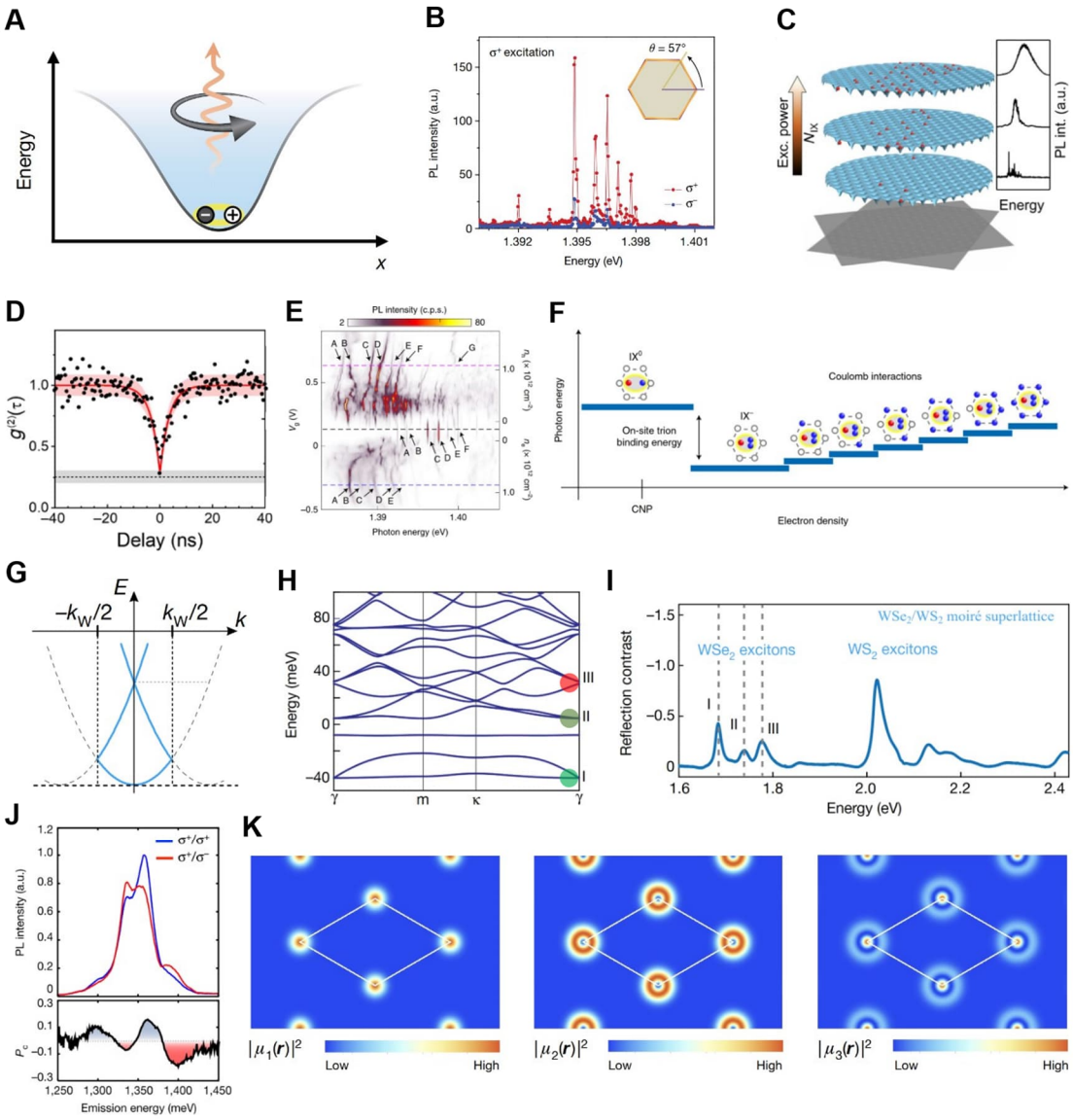

Fig. 2. Moiré excitons and trions. (**A**) Representation of an exciton trapped at the moiré potential minima. (**B**) Circularly polarized PL spectra of moiré trapped IXs of 57° $MoSe_2/WSe_2$ heterostructures. (**C**) Schematic of the occupation of moiré sites by IXs with increasing excitation power. (**D**) Second-order photon correlation statistics of moiré-trapped IXs. The antibunching indicates the single-photon nature. (**E**) PL map as a function of doping. At electron/hole doping, moiré-trapped trions with lower energy emerge. The prominent IX emissions are labelled as A-G. (**F**) Schematic of the moiré-trapped IX energy against electron density. Successive filling of nearest-neighbour moiré sites leads to a Coulomb staircase. (**G**) Sketch depicting the exciton band folding by umklapp scattering off moiré potential. (**H,I**) Calculated WSe_2 A exciton dispersion of WS_2/WSe_2 moiré superlattices, with three optically allowed transitions denoted I–III (**H**), which are observed by reflectance contrast spectrum (**I**). (**J**) Helicity-resolved PL spectra of 1° $MoSe_2/WSe_2$ heterobilayers, with alternating circular polarization. (**K**) Real-space map of the centre-of-mass wavefunctions for the first three umklapp moiré IXs. Adapted with permission from: **A** and **B**, Ref.(19), **C**, Ref.(69), **D**, Ref.(23), **E** and **F**, Ref.(74), **H** and **I**, Ref.(20), **J** and **K**, Ref.(21).

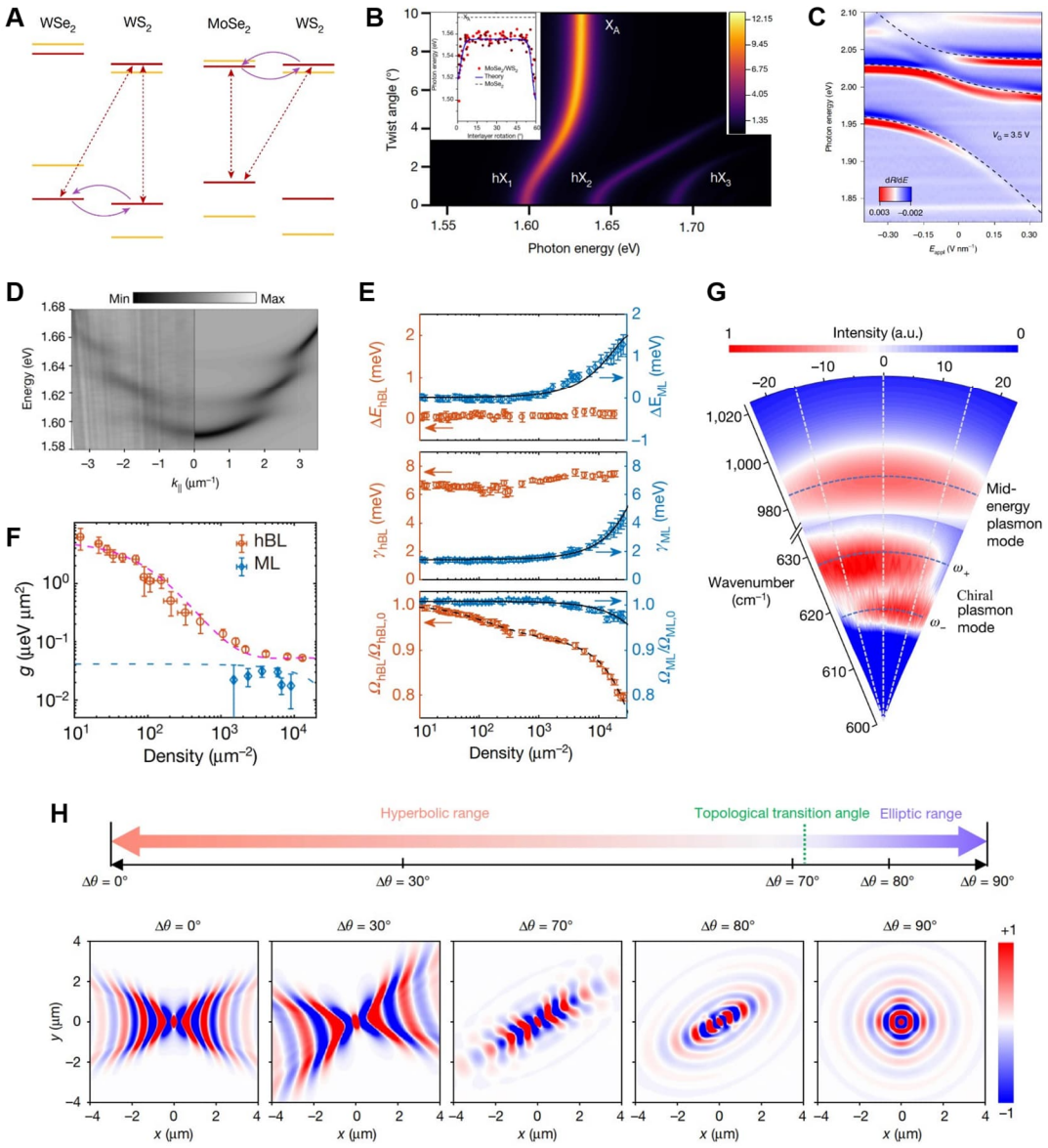

Fig. 3. Resonantly hybridized excitons and moiré polaritons. (**A**) Schematic diagram of resonantly hybridized excitons resulting from the interlayer hole (right) and electron hopping (left). (**B**) Calculated absorption spectrum of resonantly hybridized exciton versus twist angle in $MoSe_2/WS_2$ moiré superlattices, which is demonstrated by PL measurements (inset). (**C**) Derivative of the reflectance spectrum against the electric field in 60° aligned WS_2/WSe_2 moiré superlattices. (**D**) Angle-resolved reflectance spectra, demonstrating strong coupling between resonantly hybridized excitons and cavity photons. (**E**) Carrier density dependent shift of exciton energy (upper), half-linewidth (middle), and normalized coupling strength (lower) for lower polaritons (LPs) of $MoSe_2/WS_2$ moiré superlattices (denoted as hBL) and monolayer $MoSe_2$ (denoted as ML). (**F**) Nonlinear coefficient, *g*, as a function of carrier density for moiré hBL LPs (red) and ML LPs (blue). (**G**) Extinction mapping of chiral Berry plasmons against wavenumber and polarization detection angle, demonstrating the magnetic-field-free Faraday effect. (**H**) Topological transitions triggered by the twist angle from open (hyperbolic) to closed (elliptical) dispersion contours in bilayers of α-MoO_3. Adapted with permission from: **B**, Ref.(22), **C**, Ref.(91), **D-F**, Ref.(101), **G**, Ref.(104), **H**, Ref.(108).

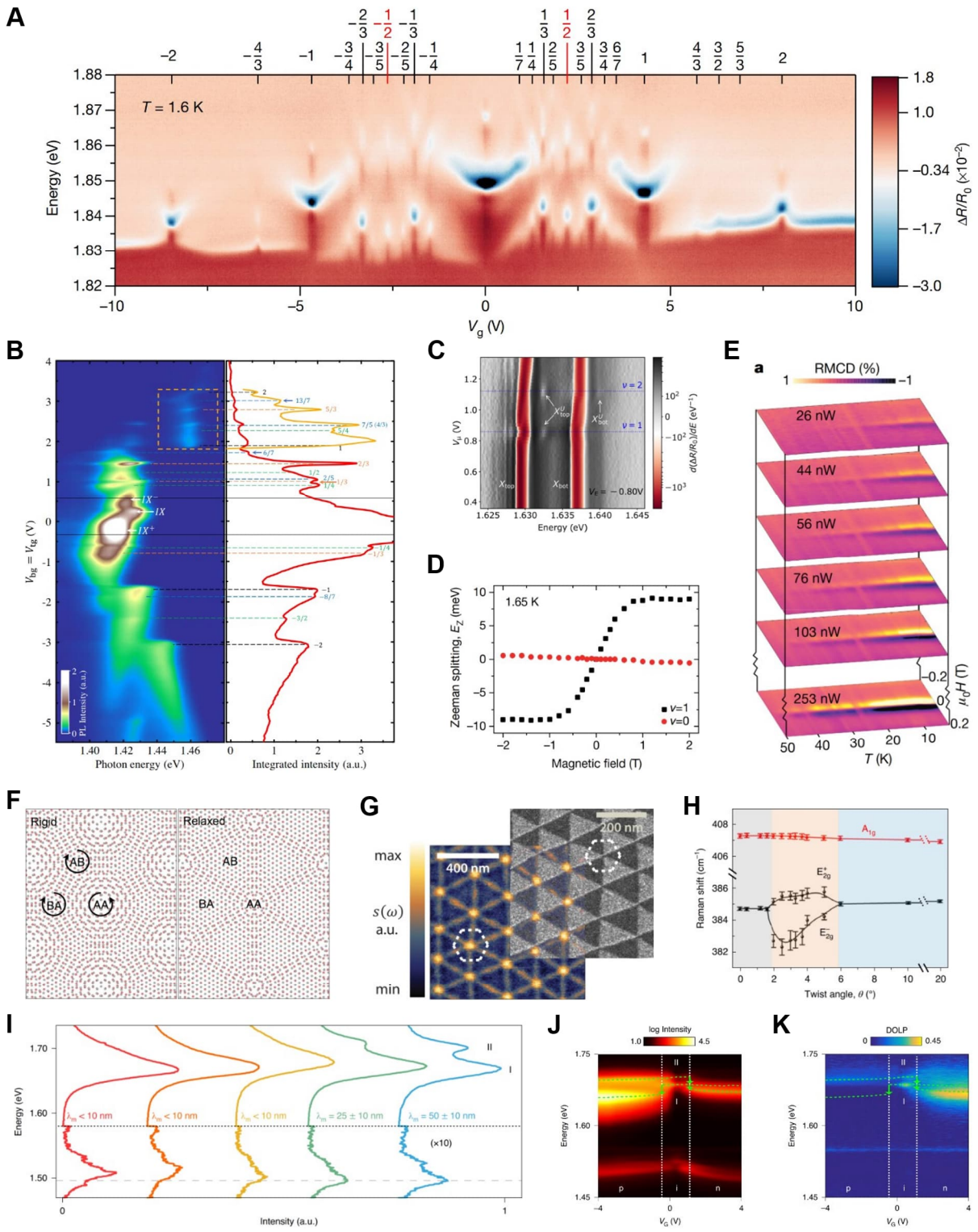

Fig. 4. Photonics of moiré correlated states and reconstructed moiré superlattices. (**A**) An abundance of correlated insulating states revealed in WSe_2/WS_2 moiré superlattices by optical sensing technique with 2s exciton resonance. (**B**) Gate-dependent PL map (left) and integrated intensity (right) for the IX states in a WS_2/WSe_2 moiré superlattice. (**C**) Dependence of chemical potential of differential reflectance differentiated with respect to energy. Umklapp exciton resonances XU top and XU bot can be clearly observed at $\nu = 1$ and $\nu = 2$. (**D**) Exciton valley

Zeeman splitting as a function of the magnetic field at zero filling (red circles) and half-filling (black squares). (**E**) Reflective magnetic circular dichroism (RMCD) as a function of magnetic field and temperature at selected excitation power, indicating light-induced ferromagnetism. (**F**) Schematic cartoon of TBG moiré superlattices with (right) and without (left) the lattice reconstruction. (**G**) Infrared nano-imaging (left) and dark-field TEM visualization (right) of TBG moiré superlattices, demonstrating a natural plasmon photonic crystal. (**H**) The energies of intralayer phonon modes versus twist angle. Clear peak splitting of E_{2g} mode can be observed at $2° \leq \theta < 6°$, providing information on reconstructed collective excitations. (**I**) PL spectra of twisted bilayer WSe_2 collected from the locations with different moiré wavelengths. A higher-energy exciton peak (type II) emerges with increasing moiré wavelength. (**J,K**) Gate-dependent PL intensity (**J**) and linear polarization (DOLP) of reconstructed twisted WSe_2 bilayers (**K**), showing distinct gate tunability and valley coherence properties. Adapted with permission from: **A**, Ref.(11), **B**, Ref.(114), **C**, Ref.(116), **D**, Ref.(43), **E**, Ref.(120), **F**, Ref.(121), **G**, Ref.(61), **H**, Ref.(124), **I-K**, Ref.(59).

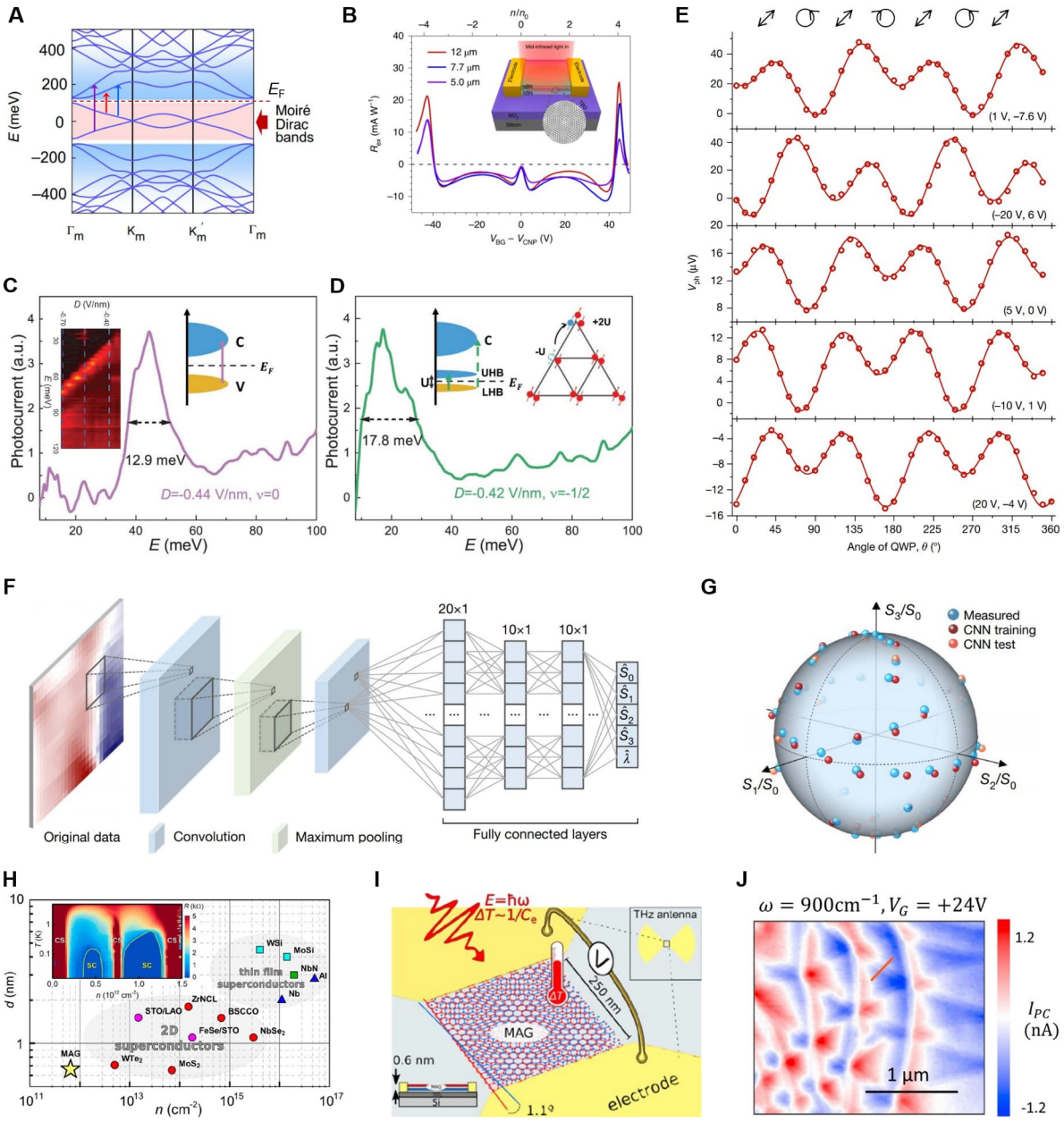

Fig. 5. Moiré optoelectronics. (**A**) Calculated band structure of 1.81° TBG, showing superlattice-induced bandgaps below and above moiré Dirac bands. (**B**) Photoresponses of TBG moiré superlattices at 5.0 μm, 7.7 μm and 12 μm light illumination. Inset: schematic diagram of moiré superlattice device for photocurrent measurement. (**C,D**) The photocurrent spectra of ABC trilayer graphene/*h*-BN moiré superlattices at zero-filling (**C**) and half-filling of the flat valence band (**D**). Photocurrents in (**C**)/(**D**) are dominated by a sharp peak at ~45 meV/a broad peak at ~18 meV, corresponding to excitation between moiré conduction and valence minibands/the emerging Mott gap, as illustrated by the inset. The inset on the right in (**D**) shows the optical transition across the Mott gap. (**E**) Photovoltage against the angle of a quarter-wave plate (QWP) at different gate voltage biases. (**F**) Schematic diagram of the convolutional neural network used for detection of the full-Stokes and wavelength. (**G**) Comparison of the polarization states obtained from convolutional neural network outputs (red/orange spheres for training/test data) with those directly measured values (blue spheres), showing high accuracy. (**H**) Comparison of carrier density and

thickness between superconductor magic-angle TBG and 2D/thin film superconductors below 10 nm. Inset: phase diagram of magic-angle TBG. (**I**) Schematic cartoon of magic-angle TBG superconducting single-photon nanocalorimeter. (**J**) Nano-imaging photocurrent of TBG moiré superlattice. Adapted with permission from: **A**,**B,** Ref.(126), **C,D,** Ref.(127), **E-G,** Ref.(33), **H,I,** Ref.(134), **J,** Ref.(135).

Table 1 | Comparison between the visualization methods of moiré superlattices		
	Pros	Cons
Atomic-resolution techniques (such as TEM and STM)	1. Directly image the local displacement vector. 2. Direct visualization of the structural relaxation, disorder and strain fields. 3. Directly visualize the magnitude of the moiré potential (for STM).	1. Require specialized sample preparation. 2. Require extreme conditions (e.g., ultra-high vacuum and low temperature). 3. Incompatible with most device fabrication techniques and optical/transport measurements.
AFM-based techniques (such as PFM, SKPM and conductive AFM)	1. Simple, room-temperature, ambient method. 2. Universal applicability. 3. Provide the key information of flexoelectricity (for PFM), surface potential (for SKPM) and interlayer hybridization (for conductive AFM).	1. Require direct contact with the active area and is incompatible with encapsulated samples. 2. Cannot image the local displacement vector. 3. Require conducting substrates (for conductive AFM).
Near-field techniques (such as SNOM, sMIM tip-enhanced Raman)	1. Ambient conditions. 2. Compatible with functional electronic devices.	Cannot image the local displacement vector.
Secondary electron imaging technique	1. Compatible with encapsulated samples and optical/transport measurements. 2. Universal applicability.	1. Cannot image the local displacement vector. 2. Cannot give the local stacking order.